Biomaterials 35 (2014) 3309–3318

Contents lists available at ScienceDirect

Biomaterials

journal homepage: www.elsevier.com/locate/biomaterials

NIR-light-induced surface-enhanced Raman scattering for detection and photothermal/photodynamic therapy of cancer cells using methylene blue-embedded gold nanorod@SiO_2 nanocomposites

Sun-Hwa Seo [a], Bo-Mi Kim [a], Ara Joe [a], Hyo-Won Han [a], Xiaoyuan Chen [b], Zhen Cheng [c], Eue-Soon Jang [a,*]

[a] Department of Applied Chemistry, Kumoh National Institute of Technology, Gyeongbuk 730-701, Republic of Korea
[b] National Institute of Biomedical Imaging and Bioengineering (NIBIB), National Institutes of Health (NIH), Bethesda, MD 20892, USA
[c] Molecular Imaging Program at Stanford (MIPS) and Bio-X Program, Department of Radiology, Stanford University, 1201 Welch Rd, Stanford, CA 94305, USA

ARTICLE INFO

Article history:
Received 19 November 2013
Accepted 20 December 2013
Available online 11 January 2014

Keywords:
Methylene blue
Gold nanorod
SERS imaging
Photodynamic therapy
Photothermal therapy

ABSTRACT

Methylene blue-loaded gold nanorod@SiO_2 (MB-GNR@SiO_2) core@shell nanoparticles are synthesized for use in cancer imaging and photothermal/photodynamic dual therapy. For the preparation of GNR@SiO_2 nanoparticles, we found that the silica coating rate of hexadecylcetyltrimethylammonium bromide (CTAB)-capped GNRs is much slower than that of PEGylated GNRs due to the densely coated CTAB bilayer. Encapsulated MB molecules have both monomer and dimer forms that result in an increase in the photosensitizing effect through different photochemical pathways. As a consequence of the excellent plasmonic properties of GNRs at near-infrared (NIR) light, the embedded MB molecules showed NIR light-induced SERS performance with a Raman enhancement factor of 3.0×10^{10}, which is enough for the detection of a single cancer cell. Moreover, the MB-GNR@SiO_2 nanoparticles exhibit a synergistic effect of photodynamic and photothermal therapies of cancer under single-wavelength NIR laser irradiation.

1. Introduction

According to cancer statistics published by the American Cancer Society, 580,350 Americans will die by cancer in 2013, which corresponds to approximately 1600 cancer deaths per day [1]. Fortunately, cancer death rates have continuously decreased by 1.7% per year owing to the rapid evolution of diagnostic instruments, biomedical technology, and nanoscience [1]. Early diagnosis of cancer, in particular, plays a crucial role in increasing the chances of survival, and molecular imaging technology based on nanoscience has emerged as a new paradigm for cancer diagnosis [2]. Typically, fluorescent semiconducting quantum dots (QDs) have received much attention as molecular imaging cancer biomarkers over the past two decades since fluorescence microscopy is a rapid and economical procedure as compared to other non-invasive imaging methods such as magnetic resonance imaging (MRI), computed tomography (CT), and positron emission tomography (PET) [3]. However, the dissolution of the heavy metal ions of QDs through the metabolism process could induce serious problems in human health, in spite of the excellent fluorescence properties of QDs. Therefore, non-cytotoxic materials such as gold, iron oxide, and silica nanoparticles are becoming the materials of choice for biomedical applications [4,5]. Among them, plasmonic gold nanoparticles have been one of the most promising materials for nanomedicine owing to their high biocompatibility and well-defined optical properties [6–8]. Especially, surface-enhanced Raman scattering (SERS) technology based on gold nanostructures has been recognized as an alternative to QD-based fluorescence imaging method because gold nanoparticles can induce enhancement of the Raman signal by a factor of 10^8–10^{14}, narrow the Raman peak width more than fluorescence peaks by 1–2 orders of magnitude, and little photobleaching effect [9,10]. As a result, numerous studies on gold nanoparticle-based SERS imaging have been reported [6,8–10]. This SERS effect of metal nanostructures is associated with surface plasmon resonance (SPR), which is the collective free electron oscillation driven by resonant electromagnetic radiation, and the wavelength used for the SPR is strongly related to their shape and size. [7,11,12] As compared to spherical gold nanoparticles, which exhibit SPR at wavelengths in the visible light range, anisotropically grown gold nanorods (GNRs) have a strong longitudinal SPR (LSPR) mode along the elongated [001] direction under near-infrared (NIR) light and their absorption

* Corresponding author.
E-mail address: euesoon@kumoh.ac.kr (E.-S. Jang).

0142-9612/$ – see front matter © 2014 Elsevier Ltd. All rights reserved.
http://dx.doi.org/10.1016/j.biomaterials.2013.12.066

wavelength can be finely tuned by controlling the aspect ratio of the GNR [11,12]. NIR light is well-known for providing a "therapeutic window" into biological tissue due to its much longer penetration depth than visible or infrared light [13]. For that reason, GNRs have drawn more attention for biomedical applications than other gold nanostructures.

In addition to excellent SERS performance, the longitudinal plasmonic response of GNRs can be rapidly converted into thermal energy as a result of lattice oscillation through electron–phonon coupling [14]. This photothermal conversion of the plasmonic response of GNRs could offer an extraordinary therapeutic approach for various malignant and nonmalignant diseases [8,15]. Consequently, GNRs have potential in terms of developing theranostics without complicated hybridization procedures to fabricate nanoparticles with different physicochemical properties [16]. However, photothermal therapy may sometimes fail to completely annihilate solid tumors because it can trigger a cytoprotective pathway in cancer cells in response to physicochemical stresses, e.g., the expression of heat-shock proteins (HSPs) [17]. The surviving cancer cells could exhibit thermo-tolerance and chemotherapy resistance and thus become more difficult to eradicate. Therefore, development of a complementary therapeutic method based on the GNR system is strongly recommended to achieve increasing anticancer efficacy.

Photodynamic therapy (PDT) is another photon-induced therapeutic method that uses a photosensitizer, but one of the major drawbacks in current PDT therapy is caused by resonant light wavelengths below 700 nm and the difficulty in preparing a water-soluble photosensitizer due to the hydrophobic structure of the photosensitizer [18]. Methylene blue (MB) is not only a water-soluble phenothiazine photosensitizer with a high quantum yield of singlet oxygen ($^1O_2$) generation ($\phi_\Delta \sim 0.5$), but it is also a popular cationic dye for histological and bacteriologic staining owing to its prominent blue color [19]. Moreover, MB is very useful as an FDA-approved drug to treat methemoglobinemia, as an antimicrobial agent for treating urinary tract infections, and as an anti-parasitic agent for treating malaria infection [20,21]. Additionally, recent studies have suggested that MB could be used as an antagonist against heat-shock response gene expression in cancer cells [22]. From an economic point of view, its low price also facilitates its use in practical applications.

In the present study, the positive charge of MB is easy to make a complex with the negatively charged GNR through electrostatic interactions. However, the PDT efficacy of MB could be restricted by using visible excitation light, as explained above. In this regard, converting the visible wavelength to NIR light is mandatory for PDT using MB. Nevertheless, relatively little research has been conducted in this direction, in contrast to the voluminous existing database on photosensitizer-incorporated multifunctional nanoparticles for cancer theranostics [23,24]. Hybridization with GNRs could solve the limitations of MB-based PDT therapy because the NIR light facilitates electron transfer from the GNRs to the MB molecules. Moreover, the synergistic effect of photothermal therapy and PDT could allow us to make considerable advances in fighting against cancer.

Herein, we demonstrate the feasibility of MB-embedded GNR@SiO_2 (MB-GNR@SiO_2) nanocomposites as a theranostic platform for SERS cancer imaging and a NIR light-induced synergistic cancer therapy combining PDT and photothermal therapy. Unlike conventional PDT techniques, one of the most promising advantages of the present MB-GNR@SiO_2 nanoparticles is the photosensitizing response of the incorporated MB molecules *via* the NIR light through plasmonic electron transfer from the GNRs. Therefore, the cancer-killing efficacy of the present MB-GNR@SiO_2 nanocomposites could be significantly enhanced as compared to that of bare GNRs. To the best of our knowledge, the present study provides empirical evidence of the enhanced SERS and cancer-killing effect of the MB-GNR@SiO_2 nanostructure.

2. Materials and methods

2.1. Synthesis of GNR solution

The GNRs were prepared by following the seed-mediated procedure developed by Murphy and coworkers [25]. The seed solution was synthesized by mixing 5 mL of 0.2 M hexadecylcetyltrimethylammonium bromide (CTAB) aqueous solution with 5 mL of 0.5 mM hydrogen tetrachloroaurate(III) tetrahydrate ($HAuCl_4 \cdot 4H_2O$), after which 0.6 mL of ice-cold 0.01 M $NaBH_4$ was added with vortex mixing for 2 min. The resulting seed solution became brownish yellow, which was then aged for 30 min at room temperature before use. For the GNR growth solution, 100 mL of 1 mM $HAuCl_4 \cdot 4H_2O$ (50 mL) was mixed with 100 mL of 0.2 M CTAB solution. Then, 4 mM of $AgNO_3$ (5 mL) and 7.9 mM of ascorbic acid aqueous solution (1.4 mL) were subsequently added under mild stirring, which changed the color from dark yellow to colorless. As the final step, 240 μL of the seed solution was added into the growth solution with gentle stirring, which changed the color to dark red within 1 h. The excess CTAB surfactant was discarded from the final product by centrifugation at 15,000 rpm for 30 min and then the precipitate was re-dispersed in 20 mL of distilled and de-ionized (DI) water with a resistivity of 18 MΩ cm. The final Au concentration of the GNR solution was measured to be 92.7 μg Au/mL by inductively coupled plasma optical emission spectrometry (ICP-OES, Varian/720-ES, USA) analysis.

2.2. Preparation of MB-GNR@SiO_2 core@shell nanoparticles

A mesoporous silica coating on GNR was achieved by the Gorelikov and Matsuura protocol [26]. Two hundred microliters (200 μL) of 0.1 M NaOH solution was added to 30 mL of the as-prepared GNR solution. Then, 20 μL of 20% tetraethylorthosilicate (TEOS) in methanol solvent was injected three times in 30 min intervals under gentle stirring. Growth of the mesoporous silica layer was allowed to continue with vigorous stirring at 600 rpm for 3 days at 30 °C. The remaining excess reagents in the resulting product were removed by centrifugation and washing three times with methanol. The purified GNR@SiO_2 was dispersed in DI water and then PEGylated by using poly(ethylene glycol) methyl ether thiol (*m*PEG-SH, MW: 1000, Sigma–Aldrich) to enhance the stability. The resulting GNR@SiO_2 solution was mixed with excess MB (0.2 g) under stirring for 3 days at room temperature. In order to completely eliminate the physically adsorbed MB molecules, the MB-loaded GNR@SiO_2 solution was repeatedly centrifuged and washed with DI water until the supernatant solution changed color from dark blue to colorless. From the ICP-OES analysis, Au concentration of the MB-GNR@SiO_2 solution was determined to be 94.8 μg Au/mL.

2.3. Characterization

The morphology of the prepared nanoparticles was confirmed by using a JEM 2100 (JEOL, Japan) transmission electron microscope (TEM) operating at 200 kV. The UV–Vis absorption spectra of the nanoparticle solution were acquired using Optizen 3220UV (Mecasys, Korea). Micro-Raman spectra with 514 nm (10 mW, 1 μm spot size) and 785 nm (0.05 mW, 1 μm spot size) excitation were obtained by an inVia Raman microscope system (Renishaw, UK) equipped with a Leica DM 2500 microscope (Leica, Germany) using a 1200 g/mm grating.

2.4. Cell culture and cellular uptake of nanoparticles

CT-26 mouse colon cancer cells from Korean Cell Line Bank (KCLB) were cultured in maintenance medium consisting of Dulbecco's Modified Eagle Medium (DMEM) (1000 mg/L glucose, Gibco), 10% fetal bovine serum (FBS, Invitrogen), and 100 U/mL penicillin–streptomycin sulfate (Welgene) at 37 °C in a humidified atmosphere with 5% CO_2. The CT-26 cancer cells (7×10^4 cells/well) were seeded in a 48-well culture plate and cultured overnight. After adding the MB-GNR@SiO_2 nanoparticles (3.3 μg Au to each well), the resulting CT-26 cells were maintained for 2 h in a 5% CO_2 incubator at 37 °C. The cells were then washed three times with phosphate-buffered saline (PBS, pH 7.4). The nanoparticle-labeled CT-26 cells were observed by a dark-field inverted microscope (Ti–S, Nikon).

2.5. Cellular toxicity of the MB-GNR@SiO_2 nanoparticles

To examine the biological effects of the MB-GNR@SiO_2 nanoparticles and GNRs on the CT-26 cancer cells in terms of cell viability, we performed the colorimetric MTT [3-(4,5)-dimethylthiahiazo-2-yl-2,5-diphenyltetrazolium bromide] metabolic activity assay using an Epoch™ microplate spectrophotometer (BioTek, USA).

2.6. Photothermal and photodynamic experiment

A continuous wave laser (Changchun New Industries Optoelectronics Tech., China) with a wavelength of 780 nm and power density of 1 W/cm^2 was irradiated upon MB (20 μM/well), GNR (3.3 μg Au/well), and MB-GNR@SiO_2 (3.3 μg Au/well) transfected CT-26 cells. Upon laser irradiation, real-time detection of increasing

temperature in the cancer cells was recorded by an IR-thermo camera (SE/A325, FLIR systems Inc.) controlled with a PC program. The cellular viability of the resulting cancer cells was confirmed by MTT assay. The reactive oxygen species (ROS) level in the NIR laser-irradiated cancer cells was measured through ROS staining with DCF-DA dye by dark-field inverted fluorescence microscope (Eclipse Ti–S, Nikon).

3. Results and discussion

3.1. Characterization of materials

Fig. 1(a) shows a TEM image of the as-prepared GNRs, which have an aspect ratio of approximately 3–4. Based on recent crystallographic studies, the GNRs prepared *via* the seed-mediated growth method have rounded rectangular ends with {250} side facets because of the surface reconstruction process that takes place in order to minimize the growth of the thermodynamically unfavorable {110} facets [27]. The high-resolution TEM image shown in the inset of Fig. 1(a) illustrates the typical round-ended morphology of the current GNRs. As shown in Fig. 1(b), a silica layer with a thickness of approximately 10 nm homogeneously coated the GNRs through the modified Stöber method developed by Gorelikov and Matsuura [26]. Typically, the Stöber method is a well-known procedure for preparing silica-coated nanoparticles under a hydrophilic solvent (e.g. ethanol), but this method is difficult to apply directly in CTAB-coated GNRs [28]. Because weakly bonded CTAB molecules can be easily removed from the GNR surface under an ethanol solvent, severe aggregation of the GNRs usually occurs [29]. Substitution of CTAB molecules with a stabilizing ligand such as thiolated polyethylene glycol (*m*PEG-SH) could result in ethanol-dispersed GNRs [30]. However, such an intermediary surfactant-coating step was not needed in the present modified Stöber process. Moreover, the CTAB-covered GNRs have a different site-selective silica coating pathway with *m*PEG–SH-covered ones as documented by Wang et al. [31] Namely, the silica layer on a CTAB-stabilized GNR surface was selectively coated at the GNR ends densely covered by the CTAB bilayer; however, the silica coated the side surface prior to the end facets for the *m*PEG–SH-modified GNR. We obtained the same results for the *m*PEG–SH-conjugated GNRs, but preferential silica coating on the end surfaces was not observed with the CTAB-attached GNRs (please see Fig. S1 in the Supporting Information). Wang et al. utilized *m*PEG-SH with a high molecular weight (MW = 5000) as a substitute for CTAB molecules on the GNR surface, such that the long chain length of *m*PEG-SH could lead to large steric hindrance as a consequence of increasing flocculation force [30]. In the present study, we used an *m*PEG-SH polymer with a low molecular weight (MW = 1000), which enabled effective substitution of the CTAB molecules on the side surfaces of the GNRs and facilitated the hydrolysis reaction of TEOS. One of the outstanding features in the present study is that the silica-coating rate for the CTAB-stabilized GNRs is much slower

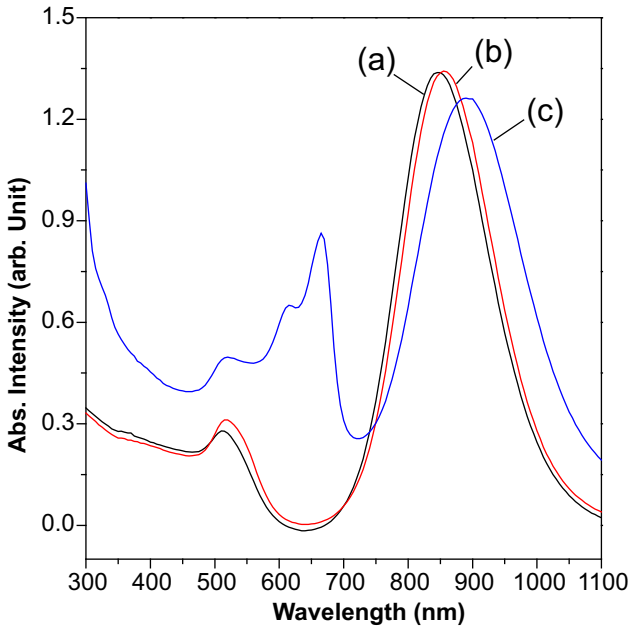

Fig. 2. UV–Vis absorption spectra of (a) GNR, (b) GNR@SiO_2, and (c) MB-GNR@SiO_2.

than that for the *m*PEG–SH-modified GNRs because a thick silica layer above 100 nm was achieved from the PEGylated GNRs at the same concentration of TEOS (1.8 mM) and a short reaction time of 3 h as shown in Fig. 1(c). Actually, 0.22 mM of TEOS was enough for the *m*PEG–SH-modified GNRs to grow a silica layer with a thickness of 20 nm (please see Fig. S1 in the Supporting Information). This fact implies that the hydrolysis and condensation reactions of TEOS molecules on the GNR surface could be interrupted by a dense covering of CTAB molecules. However, Gorelikov suggested that exposed CTAB molecules had no influence on the hydrolysis and condensation reactions of TEOS, which is significantly different from the present results and those of Wang et al. [26,31].

Fig. 2 displays UV–Vis absorption spectra of the GNR, GNR@SiO_2, and MB-GNR@SiO_2 colloidal suspensions. Fig. 2(a) shows a strong LSPR peak centered at approximately 845 nm, which corresponds to GNRs with an aspect ratio of 3–4; this result is highly congruent with the TEM results. On the other hand, the LSPR peak of GNR@SiO_2 was slightly red-shifted to 856 nm, as shown in Fig. 2(b). This is consistent with the Mie–Gans theory, in which the plasmon wavelength of GNRs is sensitively changed by the surrounding dielectric environment (ε_m), as shown in the following equation. [7,32]

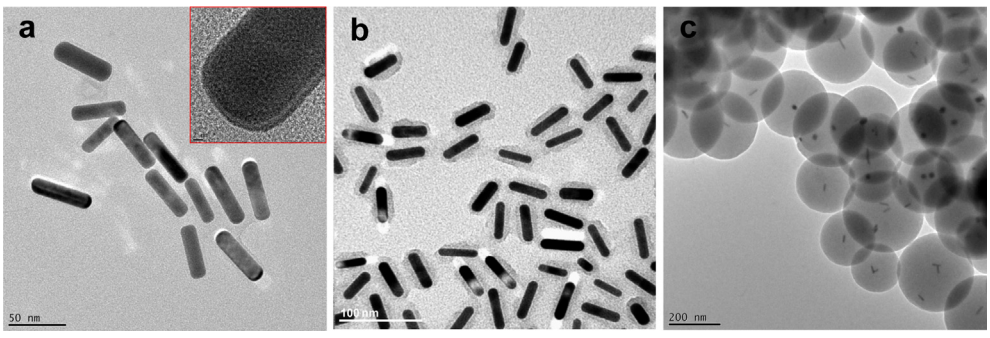

Fig. 1. TEM images of (a) bare GNRs and GNR@SiO_2 nanoparticles obtained from (b) CTAB and (c) *m*PEG–SH-covered GNRs.

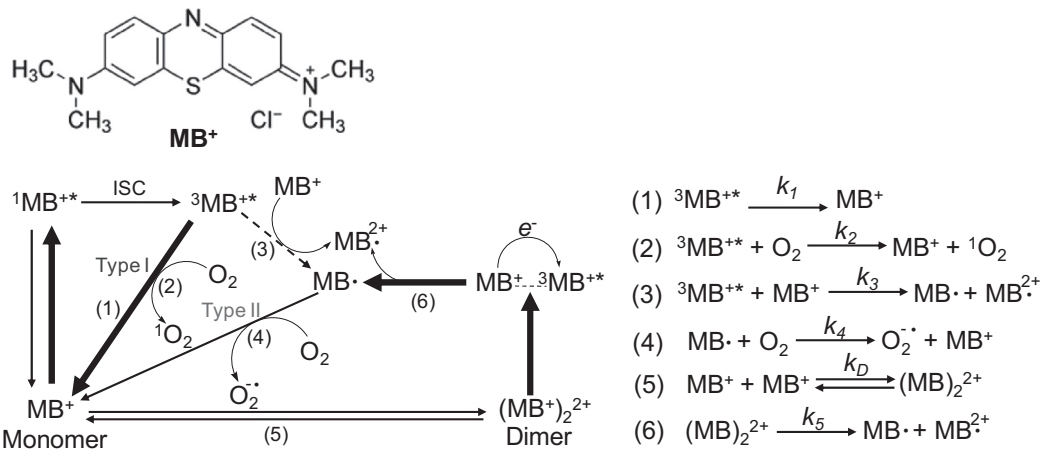

Scheme 1. Schematic illustration of photochemical reaction of methylene blue, where MB^+ is the singlet ground state; $^1MB^{+*}$ the excited singlet state; $^3MB^{+*}$ the excited triplet state; ISC the intersystem crossing; MB• the semi-reduced radical; $MB•^{2+}$ the semi-oxidized radical; O_2 the ground state triplet oxygen; $^1O_2$ the excited singlet oxygen; and $O_2^{-•}$ the semi-reduced oxygen radical. Reactions (1)–(4) represent the deactivation process of the excited triplet state ($^3MB^{+*}$) and the radical species (MB•), where reaction (1) is the spontaneous decay of $^3MB^{+*}$, (2) the oxidation decay of $^3MB^{+*}$ by triplet oxygen, (3) the reduction decay of $^3MB^{+*}$ by MB^+ or a reducing agent (e.g. GNR), and (4) the superoxide generation through oxidation decay of MB• by triplet oxygen. Reaction (5) is a self-dimerization process of the ground state MB^+ and (6) is the self-dissociation process of exciting ground state dimers. Adapted from Ref. [21] by permission from Elsevier.

$$\lambda_{GNR} = \lambda_p \sqrt{\varepsilon_o + \left(\frac{1}{L} - 1\right)\varepsilon_m} \quad (1)$$

Here, ε_0 is the high-frequency dielectric constant of gold, L is the depolarization factor along the longitudinal direction of the GNR, and ε_m is the dielectric constant of the surrounding medium. In eq. (1), λ_p is the plasma wavelength, which is determined from the electron density (N) and the effective mass of electrons (m^*) in gold, as represented in eq. (2).

$$\lambda_p = \sqrt{\frac{4\pi^2 c^2 m^* \varepsilon_o}{Ne^2}} \quad (2)$$

Namely, the increasing dielectric constant or the refractive index *via* the silica layer coating enhances the λ_{GNR} of the GNRs and eventually results in a red-shift in the LSPR wavelength for the GNR@SiO_2. For the MB-GNR@SiO_2 nanocomposites, the LSPR peak was significantly red-shifted to 892 nm from 856 nm of GNR@SiO_2, as shown in Fig. 2(c). It can be easily understood from eq. (2) that the electron transfer from the GNRs to the MB molecules leads to a decrease in the electron density of the GNRs and thus the value of λ_p increases compared to λ_p of the GNR@SiO_2 system. Such an LSPR shift of GNRs as a function of the surrounding medium has been systematically studied and described in previous reports [33,34]. On the other hand, the typical MB absorption peaks at 664 nm and 615 nm were clearly observed for the MB-GNR@SiO_2 suspension. The former and the latter absorption peaks are related to the MB monomer and dimer species, and their absorption intensity ratio ($A_{664/615}$) could provide a qualitative estimate of the relative concentration of dimers to monomers [19,35]. From the change of UV–Vis absorption spectra of the MB solution with increasing concentration from 10 μM to 1 mM, we found that the value of $A_{664/615}$ systematically decreased from 1.95 for 10 μM to 1.05 for 125 μM (please see Fig. S2(a) in the Supporting information). Eventually, a new absorption peak was observed at 555 nm for the 250 μM concentration, which corresponds to a trimer and a more aggregated MB form (Fig. S2(a)-(ix)) [35]. At 1 mM, the peak was significantly red-shifted to 517 nm, as shown in Fig. 2(S)(b)-(xi). It is a well-known fact that a homogenous MB solution with a low concentration (<20 μM) has an almost monomeric form (>93%) [19]. For the present MB-GNR@SiO_2, the $A_{664/615}$ value of 1.30 is comparable to that of 1.35 of the 40 μM MB solution even though the concentration of the loaded MB molecules was as low as 8 μM, which was determined by using a standard fitting curve from the absorption intensity observed at 664 nm of MB solutions with various concentrations (please see Fig. S2(b) in the Supporting Information). This indicates that dimer species were present among the MB molecules loaded into the GNR@SiO_2 nanoparticles. One possible reason for the dimer formation in the MB-GNR@SiO_2 may be the locally increased concentration of the MB molecules around the GNRs coated with a SiO_2 layer as compared to the concentration of free molecules in the aqueous solution. In addition, as reported by Severino et al., the MB dimer formation could be facilitated by a negatively charged interface through electrostatic interaction even at a low concentration of the MB solution [36]. Namely, the negatively charged GNR surface leads to stabilization of the MB dimer species around the GNRs.

The MB monomers and dimers have distinct photochemical reactions, as has been reported by Tardivo et al., and this could affect the cancer-killing efficacy [19]. After optical pumping, the monomers generally correspond to the type I photochemical pathway, in which photoexcited MB molecules in a singlet state undergo intersystem crossing (ISC) to a metastable triplet state with high quantum yield. Then, singlet oxygen molecules ($^1O_2$) could be generated by the triplet MB molecules through exchange energy transfer, as represented by reaction (2) in Scheme 1. By contrast, the MB dimers can produce MB free radicals as a result of self-dissociation, as shown in reaction (6) of Scheme 1. The chemical reaction between MB radicals and oxygen produces a superoxide (reaction (4)). Also, the residual MB radicals can lead to the formation of various ROS species, including a highly reactive hydroxyl radical through a Fenton reaction [37]. Therefore, MB dimers may be more effective than monomers in eliminating hypoxic tumors, which is a characteristic feature of outgrowing solid tumors as a consequence of the disproportion between oxygen supply and consumption, without photoexcitation. However, a high concentration of MB solution is usually required in order to obtain the necessary dimers, which could induce chemical toxicity in normal cells. For that reason, it is worthwhile to confirm the presence of MB dimers or more aggregated forms in the MB-GNR@SiO_2 nanocomposites in order to overcome the above mentioned drawback in conventional MB treatment.

Higher aggregated forms of MB could facilitate type II photoreaction and they have an absorption maximum around 570 nm (Fig. S2(a)-(vii)–(xi)), but the relevant absorption peak was not observed for the present MB-GNR@SiO_2. In order to further confirm the presence of higher aggregated MB molecules, micro-Raman experiments were carried out on the MB-GNR@SiO_2 suspension and the solid MB film by using a He laser source with a wavelength of 514 nm ($d_{spot} \approx 1$ μm). It is noted that the MB monomers and dimers have no absorption at 514 nm and thus we can ignore their contributions in the resonant Raman spectrum. As shown in Fig. 3(a–c), Raman peaks observed from the MB-GNR@SiO_2 solution were nearly the same as that of the MB solid film. This indicates that some of the MB molecules in the MB-GNR@SiO_2 nanoparticles have highly aggregated forms similar to a MB solid film. Typical Raman band assignments are summarized in Table 1 [38,39]. On the contrary, Raman peaks from the solid MB film under an excitation laser at 785 nm are shown in Fig. 3(d–f). A laser wavelength of 785 nm is far away from the absorption peak of the MB molecule but close to the LSPR absorption peak of the GNR. Therefore, there are no Raman modes from the solid MB film, but strong SERS peaks were observed from the MB-GNR@SiO_2 nanoparticles by irradiation with a 785 nm laser. Especially, the intensity of the C–N–C skeletal deformation mode (δ(C–N–C)) at 439 cm^{-1} (Fig. 3(d)) and the C–N symmetric stretching mode (ν(C–N)) at 1386 cm^{-1} (Fig. 3(e)) were remarkably enhanced as compared to normal Raman peaks obtained from the solid MB film under a 514 nm excitation laser (Fig. 3(a)). Moreover, the Au–N stretching mode (ν(Au–N)) newly appeared at 238 cm^{-1} from the MB-GNR@SiO_2 nanocomposites, as shown in Fig. 3(d) [39]. This is clear evidence that the loaded MB molecules were bonded to the GNR surface through nitrogen atoms, resulting in an SERS effect by transferring the plasmonic free electrons from the GNRs to the MB molecules. To estimate the SERS enhancement, we calculated the Raman enhancement factor (R_{EF})

Table 1
Raman frequencies and corresponding assignments of the main bands observed from the MB solid film and MB-GNR@SiO_2 solution by excitation at 514 nm and 785 nm.

Assignment	Solid MB	MB-GNR@SiO_2	
	λ = 514 nm	λ = 514 nm	λ = 785 nm
	Frequency, cm^{-1}		
ν(Au–N)			238
δ(C–N–C)	446	450	439
δ(C–N–C)	500	500	490
	535		540
			560
			581
δ(C–S–C)	593		596
γ(C–H)	670	671	659
	769		760
	856		875
	950		944
β(C–H)	1037	1037	1034
	1071	1069	
β(C–H)	1153	1150	1144
ν(C–N)	1184	1180	1173
ν(N–CH_3)	1223	1223	1222
	1301	1301	1295
	1362	1359	1318
ν_{sym}(C–N)	1396	1393	1386
ν_{asym}(C–N)	1438	1438	1427
ν_{asym}(C–C)	1470		1462
			1494
ν(C–C)$_{ring}$	1624	1621	1613
ν(C–C)$_{ring}$	2074		
	2107		
	2383	2369	
ν_{sym}(C–H_3)	2475	2475	
ν_{sym}(C–H_3)	2775	2777	
ν_{sym}(C–H_3)	2880	2875	

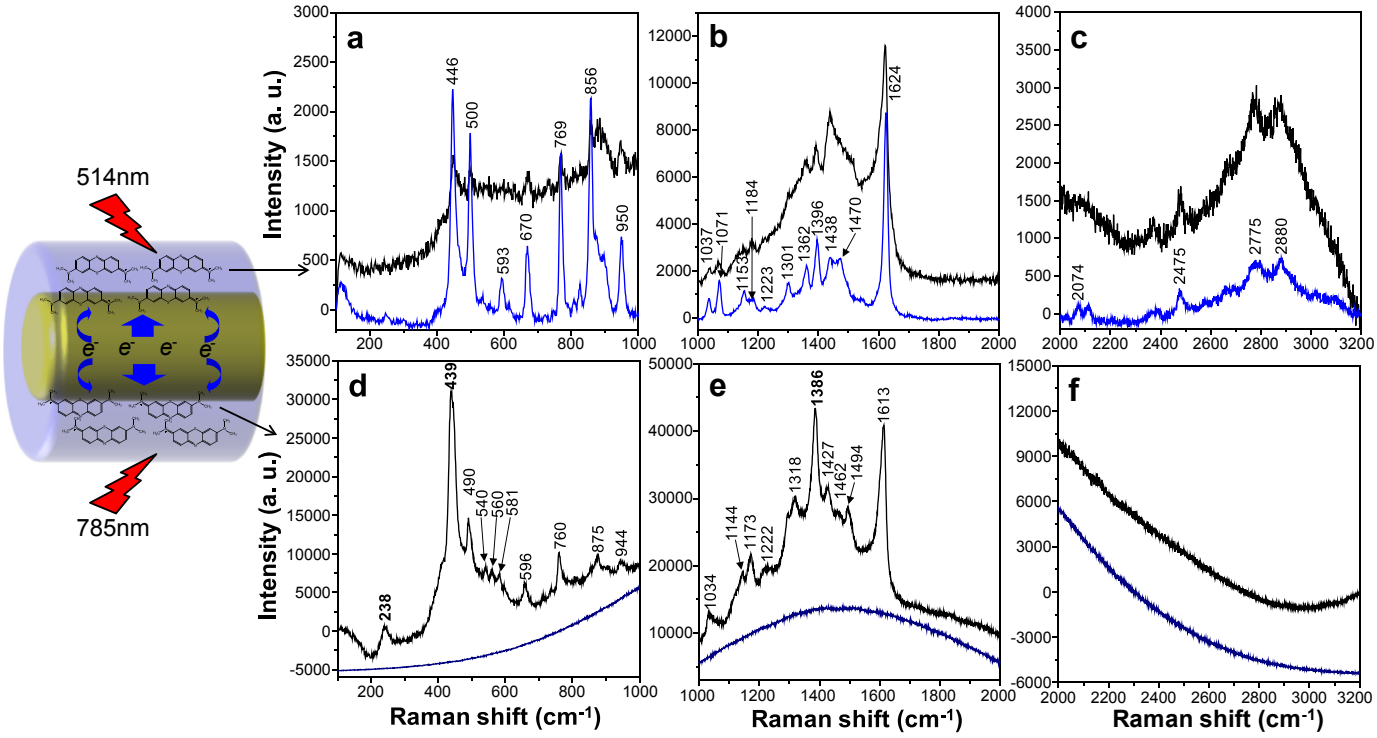

Fig. 3. Micro-Raman spectra of MB solid film and MB-GNR@SiO_2 solution excited by (a–c) 514 nm (10 mW, $d_{spot} = 1$ μm) and (d–f) 785 nm (0.05 mW, $d_{spot} = 1$ μm). Schematic illustration shows loaded MB dimers and monomers excited at 514 nm and 785 nm, respectively, in which plasmon damping electrons along the longitudinal direction transfer from the GNRs to the MB monomers by NIR resonant light pumping.

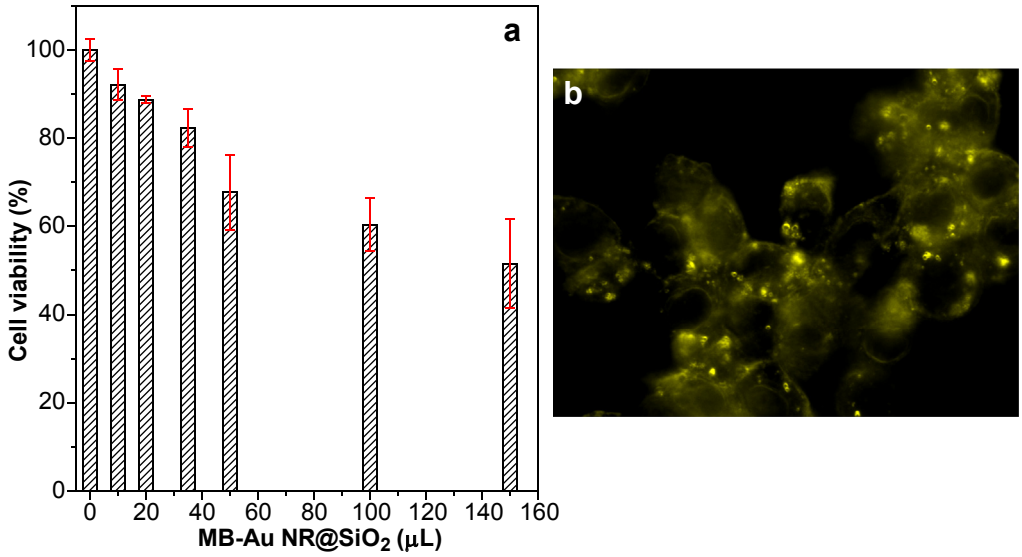

Fig. 4. (a) Chemical toxicity of MB-GNR@SiO_2 nanoparticles to cancer cells upon increasing volume (94.8 μg Au/mL) after incubation for 2 h. MTT assay was accomplished after washing residual nanoparticles and further incubation for 12 h. (b) Dark-field image of the MB-GNR@SiO_2 nanoparticle-transfected CT-26 cells (3.3 μg Au per well) after incubation for 2 h. Bright yellow color indicates the nanoparticles loaded into the cytoplasmic membrane of the cancer cells. (For interpretation of the references to colour in this figure legend, the reader is referred to the web version of this article.)

per MB molecule as the ratio of the intensity of the δ(C–N–C) mode obtained from the MB-GNR@SiO_2 nanoparticles and the solid MB film under excitation at 785 nm and 514 nm, respectively. The R_{EF} of SERS is defined as

$$R_{EF} = \frac{N_{Bulk}}{N_{Ads}} \times \frac{I_{SERS}}{I_{Raman}} \quad (3)$$

In eq. (3), N_{Bulk} is the number of MB molecules for the solid MB film and N_{Ads} is the number of MB molecules adsorbed on the GNR surfaces for MB-GNR@SiO_2 nanoparticles in the laser-activated volume. I_{SERS} and I_{Raman} are the intensities of the vibrational mode in SERS and normal Raman spectrum, respectively [40]. For the present study, the δ(C–N–C) mode at 439 cm^{-1} was utilized to estimate the R_{EF} and it was calculated to be around 3.0×10^{10}. As reported by Le Ru et al., an R_{EF} of 10^7 is sufficient to observe a single-molecule SERS signal but that of the present MB-GNR@SiO_2 nanoparticles is strongly enhanced by 1000 times [41]. Further detailed calculations are presented in the Supporting Information. In fact, we postulated that the laser penetration depth for SERS and normal Raman experiments is the same. However, the penetration depth is expected to be less for SERS conditions excited at 785 nm with a laser power of 0.05 mW as compared to normal Raman conditions excited at 514 nm with a laser power of 10 mW due to the remarkably low power density. For that reason, the real R_{EF} value of the SERS spectrum for the MB-GNR@SiO_2 nanoparticles may be higher than the above calculated values.

3.2. Determination of optimum MB-GNR@SiO_2 concentration for cancer treatment

An MTT assay was accomplished in order to determine the concentration of the MB-GNR@SiO_2 nanoparticles needed for cancer treatment while minimizing the chemical toxicity of the nanocomposites. From the ICP-OES analyses, the gold concentration of the MB-GNR@SiO_2 solution was determined to be 94.8 μg Au/mL and various volumes (0–150 μL) of the nanoparticles were added to the CT-26 cancer cells, which had a density of 7×10^4 per well. The resulting cancer cells were maintained for 2 h in a 5% CO_2 incubator at 37 °C and then further incubated for 12 h in order to investigate accurately the cellular toxicity of the MB-GNR@SiO_2-transfected CT-26 cancer cells after washing the remaining nanoparticles in the media. As shown in Fig. 4(a), cancer cell viability decreased to 52% upon increasing the dose of the MB-GNR@SiO_2 nanocomposites from 0 to 150 μL (0–14.2 μg Au). Usually, cell viability above 80% is reasonable for excluding the chemical toxicity of the transfected nanoparticles, and thus the concentration of the MB-GNR@SiO_2 nanoparticles was determined to be 3.3 μg Au per well (35 μL per well) for treatment of the CT-26 cancer cells. Namely, the chemical toxicity of the MB-GNR@SiO_2 nanoparticles is insignificant at the above concentration and therefore we can consider just the pure photothermal and photosensitizing effects of the MB-GNR@SiO_2 nanocomposites on the cancer-killing efficiency upon a resonant laser irradiation. Fig. 4(b) shows a dark-field image of the MB-GNR@SiO_2 nanoparticle-transfected CT-26 cells after incubation for 2 h. The bright yellow color indicates that the nanoparticles were loaded into the cytoplasmic membrane of the cancer cells.

3.3. SERS Spectra of MB-GNR@SiO_2-transfected cancer cell

Fig. 5 shows bright-field images and SERS spectra corresponding to the control and MB-GNR@SiO_2-transfected cancer cells under excitation laser at 785 nm. The red cross in the cancer cell photos indicates the laser-activated area. For the control cancer cells without nanoparticle treatment, a broad background originating from the DMEM cell culture media was observed (Fig. 5(a)). For the MB-GNR@SiO_2 nanoparticle-treated cancer cells, shown in Fig. 5(b), the typical δ(C–N–C), ν_{sym}(C–N), and $\nu(C–C)_{ring}$ modes of the MB molecules were clearly observed at 446, 1380, and 1605 cm^{-1}, respectively, but their intensities were weak due to the low concentration of MB detected from the single cancer cell. One the other hand, the intensities of the above three modes were remarkably enhanced by the overlapped cancer cells, as shown in Fig. 5(c). Although we did not carry out *in vivo* experiments, these results indicate that the SERS intensity of the MB-GNR@SiO_2 nanoparticles is enough to achieve an early cancer diagnosis because malignant tumors consist of a lot more cancer cells and therefore the SERS

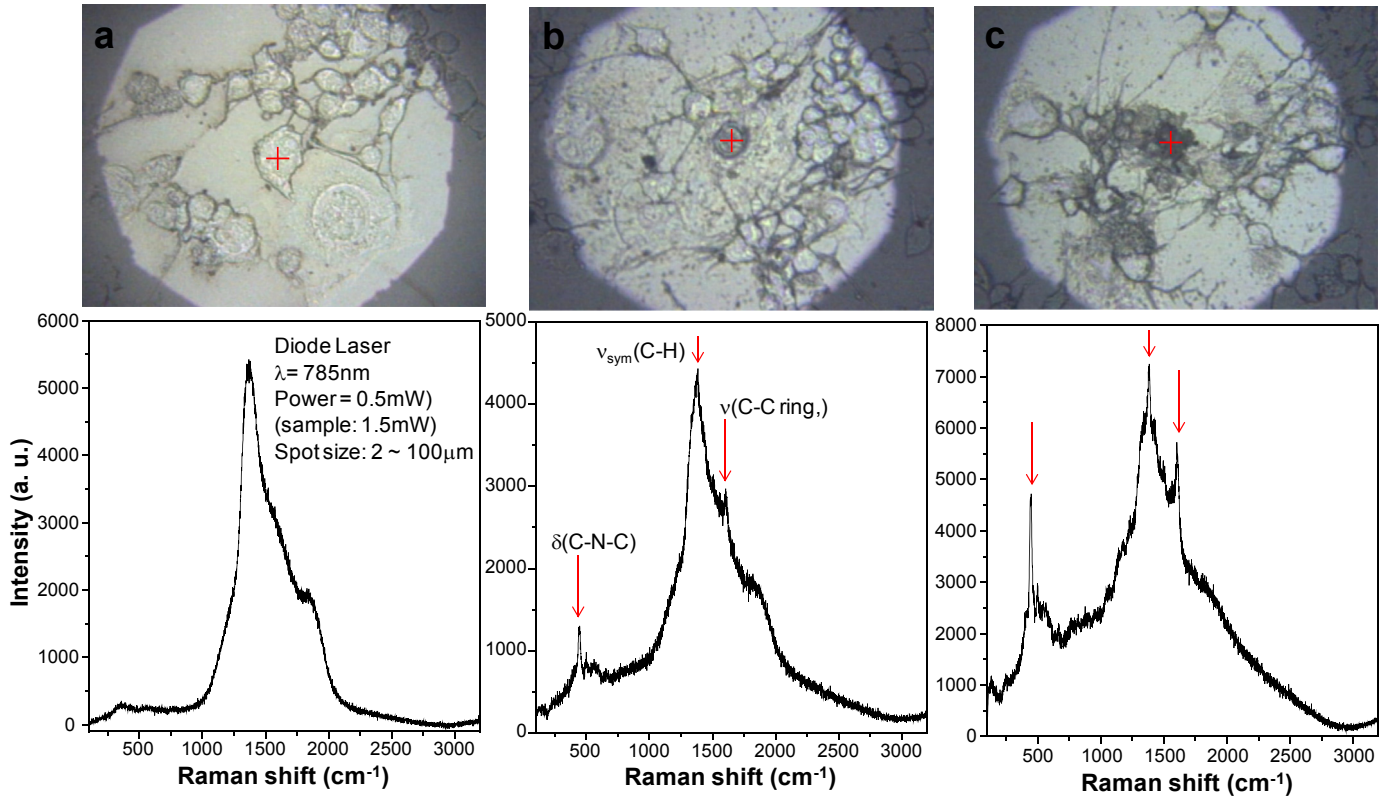

Fig. 5. Bright-field images and micro-Raman spectra of (a) control, (b) MB-GNR@SiO_2-transfected single cancer cell, and (c) MB-GNR@SiO_2-transfected agglomerated cancer cells. The red-cross in the bright-field images indicates the NIR laser-activated area (λ = 785 nm, 0.05 mW, d_{spot} = 1 μm). (For interpretation of the references to colour in this figure legend, the reader is referred to the web version of this article.)

intensity will be significantly enhanced as compared to *in vitro* cancer cell SERS imaging.

3.4. Therapeutic efficiency of MB-GNR@SiO_2 nanoparticles for cancer cells

The photothermal efficiency of the MB-GNR@SiO_2 nanoparticles was compared to that of bare GNRs without a silica coating layer and the results are shown in Fig. 6. After NIR laser irradiation (λ = 780 nm, 1 W/cm^2) for 800 s, the temperature of the MB-GNR@SiO_2 solution increased from 24 to 41 °C. This photothermal efficiency was nearly the same as that of the bare gold nanorod solution due to the thin silica thickness of 10 nm. These results indicate that the outcome through photothermal therapy using MB-GNR@SiO_2 nanoparticles is nearly the same as that using bare GNRs.

After 780 nm NIR laser irradiation, time-dependent cell viability of the bare GNR- and MB-GNR@SiO_2-transfected cancer cells was investigated by MTT assay. As shown in Fig. 7(a,b), the decrease in cell viability for the MB-GNR@SiO_2 nanoparticle-loaded cancer cells was greater than that for the bare GNR-treated cancer cells. The cell viability decreased to 31% for the GNR cells and 11% for the MB-GNR@SiO_2 cells after NIR laser irradiation for 50 min. This fact clearly implies that a synergistic combination of the photothermal and photosensitizing effects of the MB-GNR@SiO_2 nanoparticles appeared to increase cancer cell death. As shown in Fig. 8, cancer cell viability after nanoparticle treatment and laser irradiation was further confirmed by a double immunofluorescence staining study with calcein (green fluorescence) and propidium iodide (red fluorescence) dyes for live and dead cell staining, respectively. As compared to the bare gold nanorod-treated cancer cells (Fig. 8(b–f)), the live cell population of the MB-GNR@SiO_2 nanoparticle-transfected cancer cells quickly decreased upon increasing NIR laser irradiation time from 0 to 50 min (Fig. 8(g–l)). This result is well consistent with the above MTT assay results.

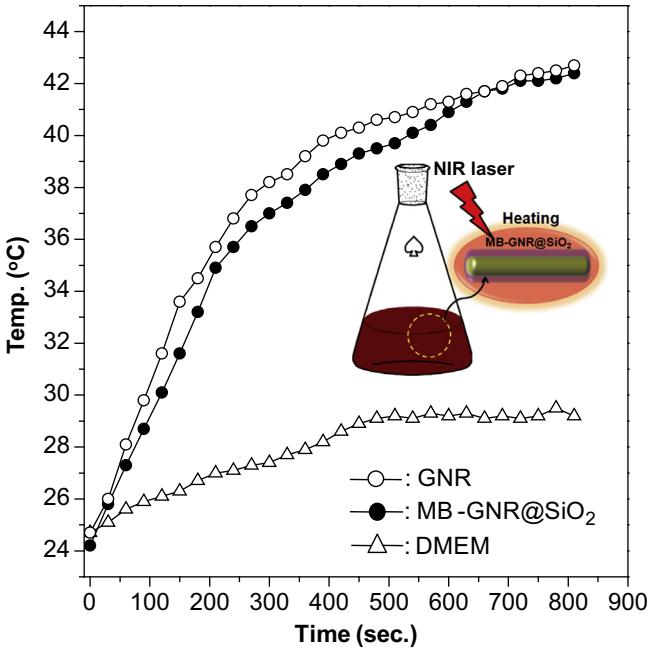

Fig. 6. Temperature variation of DMEM, GNR, and MB-GNR@SiO_2 solutions upon NIR laser irradiation (λ = 780 nm, power density = 1 W/cm^2).

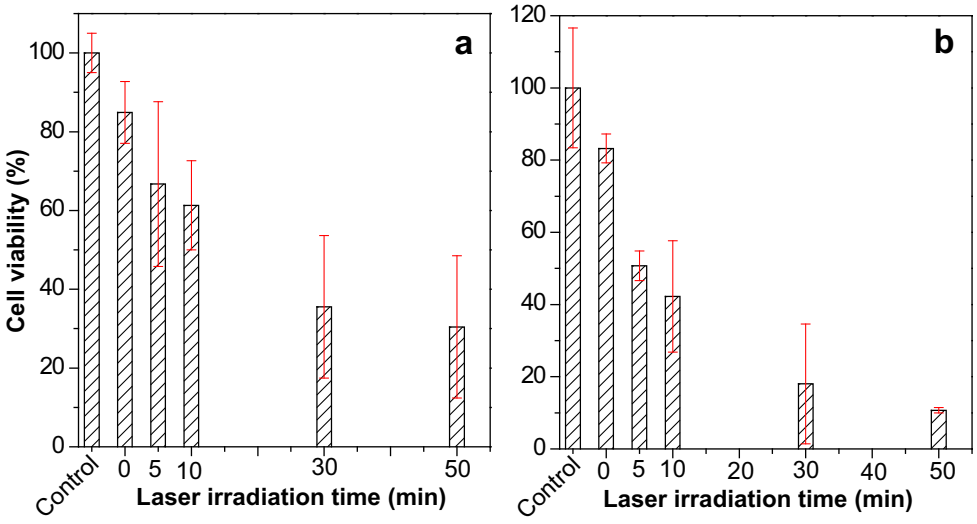

Fig. 7. Cellular viability of (a) GNR and (b) MB-GNR@SiO_2 loaded CT-26 cancer cells upon laser (λ = 780 nm, power density = 1 W/cm^2) irradiation time.

3.5. ROS Generation of MB-GNR@SiO_2-transfected cancer cells

In order to detect the ROS level in living cancer cells through the photosensitizing effect, ROS staining was carried out for the GNR-, MB-GNR@SiO_2-, and MB-transfected cancer cells upon NIR laser irradiation (λ = 780 nm, 1 W/cm^2) by using DCFH-DA as the green fluorescence dye. For the GNR-transfected cancer cells, the ROS level increased very slowly even at an irradiation time of 50 min, which seems to be a result of mitochondria degradation in response to thermal stress *via* the photothermal effect of the GNR, as shown in Fig. 9(a–d). However, for the MB-GNR@SiO_2 nanoparticle-transfected cancer cells, the ROS level was significantly enhanced with increasing NIR laser irradiation time, as shown in Fig. 9(e–h). This is clear evidence that the MB-GNR@SiO_2 nanoparticles have not only a photothermal effect but also a photosensitizing one. Moreover, the most important difference between the GNR- and MB-GNR@SiO_2 nanoparticle-loaded cancer cells is ROS generation in dark conditions, such that the green fluorescence intensity for the latter was much stronger than that for the former, as shown in Fig. 9(a,e). Such a difference in the ROS level was also observed for the cancer cells treated with MB solutions with concentrations of 10 μM and 40 μM under dark conditions, as shown in Fig. 9(i,m), respectively. This fact implies that the MB-GNR@SiO_2 nanoparticles operated according to the direct oxidation process of the MB dimers through a type II photoreaction pathway, as represented in Scheme 1. Nevertheless, the ROS signal intensity for the cancer cells treated with MB solutions with concentrations of 10 μM (Fig. 9(i–l)) and 40 μM (Fig. 9(m–p)) did not change upon increasing laser irradiation time since the wavelength of the excitation laser was far away from the absorption wavelength of the MB molecules. Therefore, for the MB-GNR@SiO_2-transfected cancer cells, it seems reasonable to assume that movement of the plasmon-induced electrons from the

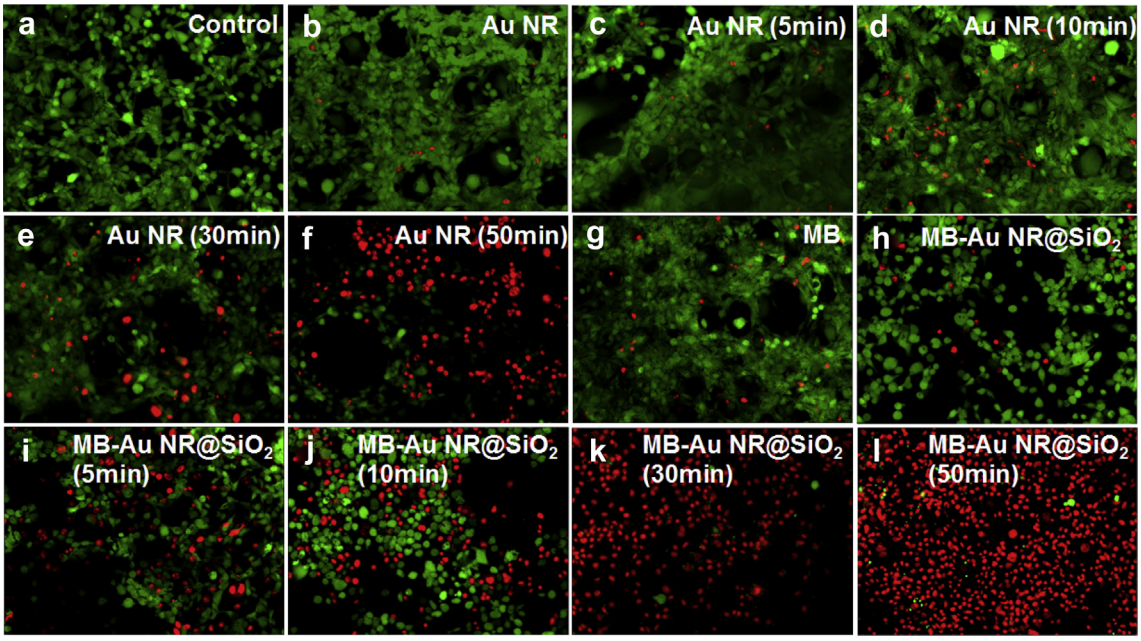

Fig. 8. Double immunofluorescence staining images of (a) control, (b–f) GNR (3.3 μg Au per well), (g) MB (20 μM), and (i–l) MB-GNR@SiO_2-treated CT-26 cancer cells (3.3 μg Au per well) as a function of NIR laser irradiation time (λ = 780 nm, power density = 1 W/cm^2).

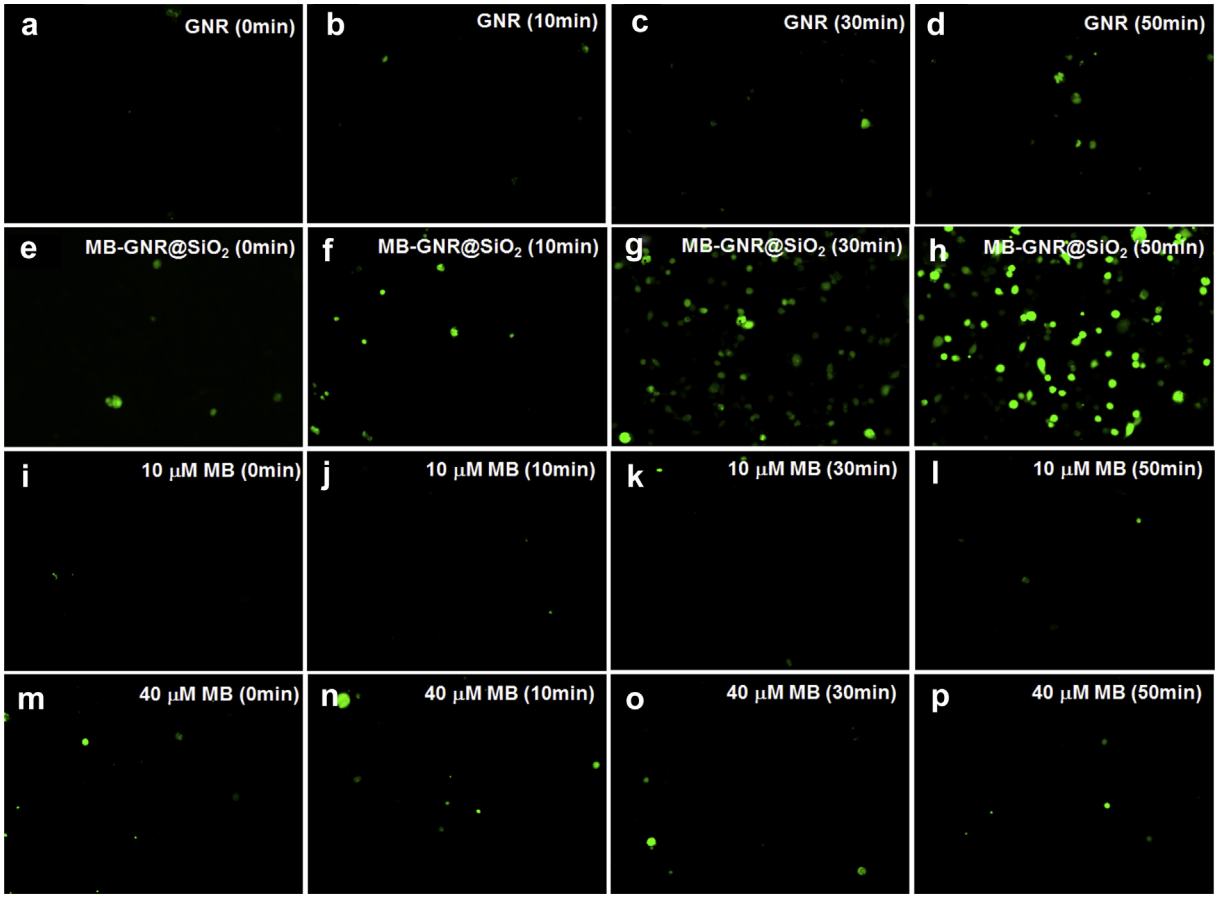

Fig. 9. ROS staining fluouresence images of (a–d) GNR (3.3 μg Au per well), (e–h) MB-GNR@SiO_2 (3.3 μg Au per well), (i–l) 10 μM MB solution, and (m–p) 20 μM MB solution-treated CT-26 cancer cells.

GNRs to the MB molecules could accelerate the ROS generation through the type I photochemical pathway, as mentioned earlier.

4. Conclusions

We successfully synthesized MB-GNR@SiO_2 nanoparticles, which showed excellent SERS performance, with a Raman enhancement factor above 3.0×10^{10}. This SERS enhancement was enough to detect both agglomerated and single cancer cells. In addition, the resulting MB-GNR@SiO_2 nanocomposites had a photon-induced dual modality of photothermal and photosensitizing effects for cancer therapy, and thus the cancer-killing efficacy was remarkably enhanced by the present nanocomposites as compared to GNRs or MB treatment. Especially, we found that the embedded MB molecules in the GNR@SiO_2 nanoparticles had both monomers and dimers, even at a low concentration of 8 μM. Consequently, ROS generation was induced from the MB-GNR@SiO_2-transfected cancer cells by the type I and type II pathways related to the photoreaction of the MB molecules. Therefore, we believe that the present study provides empirical evidence to substantiate the promising potential of MB-GNR@SiO_2 nanoparticles to significantly advance the field of cancer theranostics.

Acknowledgments

This work was supported by research fund of the Korean Ministry of Education, Science & Technology (2013-0024700) and Small & Medium Business Administration of Korea (S2072168).

Appendix A. Supplementary data

Supplementary data related to this article can be found at http://dx.doi.org/10.1016/j.biomaterials.2013.12.066.

References

[1] Siegel R, Naishadham D, Jemal A. Cancer statics, 2013. CA: Cancer J Clin 2013;63:11–30.
[2] Louie A. Multimodality imaging probes: design and challenges. Chem Rev 2010;110:3146–95.
[3] Voura EB, Jaiswal JK, Mattoussi H, Simon SM. Tracking metastatic tumor cell extravasation with quantum dot nanocrystals and fluorescence emission-scanning microscopy. Nat Med 2004;10:993–8.
[4] Yong KT, Law WC, Hu R, Ye L, Liu L, Swihart MT, et al. Nanotoxicity assessment of quantum dots: from cellular to primate studies. Chem Soc Rev 2013;42:1236–50.
[5] Wang LS, Chuang MC, Ho JA. Nanoteranostics-a review of recent publications. Int J Nanomed 2012;7:4679–95.
[6] Kong KV, Lam Z, Goh WD, Leong WK, Olivo M. Metal carbonyl-gold nanoparticle conjugates for live-cell SERS. Angew Chem Int Ed Engl 2012;124:9934–7.
[7] Chen H, Shao L, Li Q, Wang J. Gold nanorods and their plasmonic properties. Chem Soc Rev 2013;42:2679–724.
[8] Zhang Y, Qian J, Wang D, Wang Y, He S. Multifunctional gold nanorods with ultrahigh stability and tunablility for in vivo fluorescence imaging, SERS detection, and photodynamic therapy. Angew Chem Int Ed Engl 2013;52:1148–51.
[9] Jokerst JV, Cole AJ, Van de Sompel D, Gambhir SS. Gold nanorods for ovarian cancer detection with photoacoustic imaging and reaction guidance *via* Raman imaging in living mice. ACS Nano 2012;6:10366–77.
[10] Vendrell M, Maiti KK, Dhaliwal K, Chang YT. Surface-enhanced Raman scattering in cancer detection and imaging. Cell 2013;31:249–57.
[11] Ni W, Kou X, Yang Z, Wang J. Tailoring longitudinal surface plasmon wavelengths, scattering and absorption cross sections of gold nanorods. ACS Nano 2008;2:677–86.

[12] Zuloaga J, Prodan E, Nordlander P. Quantum plasmonics: optical properties and tunability of metallic nanorods. ACS Nano 2010;4:5269–76.
[13] Weissleder R, Ntziachristos V. Shedding light onto live molecular targets. Nat Med 2003;9:123–8.
[14] Huang X, El-Sayed IH, Qian W, El-Sayed MA. Cancer cell imaging and photothermal therapy in the near-infrared region by using gold nanorods. J Am Chem Soc 2006;128:2115–20.
[15] von Maltzahn G, Park JH, Agrawal A, Bandaru NK, Das SK, Sailor MJ, et al. Computationally guided photothermal tumor therapy using long-circulating gold nanorod antennas. Cancer Res 2009;69:3892–900.
[16] Zhang Z, Wang L, Wang J, Jiang X, Li X, Hu Z, et al. Mesoporous silica-coated gold nanorods as a light-mediated multifunctional theranostic platform for cancer treatment. Adv Mater 2012;24:1418–23.
[17] Sajjadi AY, Mitra K, Grace M. Expression of heat shock proteins 70 and 47 in tissues following short-pulse laser irradiation: assessment of thermal damage and healing. Med Eng Phy 2013;35:1406–14.
[18] DeRosa MC, Crutchley RJ. Photosensitized singlet oxygen and its applications. Coord Chem Rev 2002;233–234:351–71.
[19] Tardivo JP, Giglio AD, Oliveira CS, Gabrielli DS, Junqueira HC, Tada DB, et al. Methylene blue in photodynamic therapy: from basic mechanisms to clinical applications. Phtodiag Photodyn Ther 2005;2:175–91.
[20] Wendel WB. The control of methemoglobinemia with methylene blue. J Clin Invest 1939;18:179–85.
[21] Amaral L, Miguel V, Molnar J. Antimicrobial activity of phenothiazines. Vivo 2004;18:725–32.
[22] Wang AM, Morishima Y, Clapp KM, Peng HM, Pratt WB, Gestwicki JE, et al. Inhibition of Hsp70 by methylene blue affects signaling protein function and ubiquitination and modulates polyglutamine protein degradation. J Biol Chem 2010;285:15714–23.
[23] Shi S, Zhu X, Zhao Z, Fang W, Chen M, Huang Y, et al. Photothermally enhanced photodynamic therapy based on mesoporous Pd@Ag@mSiO_2 nanocarriers. J Mater Chem B 2013;1:1133–41.
[24] Wang S, Huang P, Nie L, Xing R, Ruijun Liu, Liu D, et al. Single continuous wave laser induced photodynamic/plasmonic photothermal therapy using photosensitizer-functionalized gold nanostars. Adv Mater 2013;25:3055–61.
[25] Jana NR, Gearheart L, Murphy CJ. Wet chemical synthesis of high aspect ratio cylindrical gold nanorods. J Phys Chem B 2001;105:4065–7.
[26] Gorelikov I, Matsuura N. Single-step coating of mesoporous silica on cetyltrimethyl ammonium bromide-capped nanoparticles. Nano Lett 2008;8:369–73.
[27] Park K, Drummy LF, Wadams RC, Koerner H, Nepal D, Fabris L, et al. Growth mechanism of gold nanorods. Chem Mater 2013;25:555–63.
[28] Stöber W, Fink A, Bohn E. Controlled growth of monodisperse silica spheres in the micron size range. J Colloid Int Sci 1968;26:62–9.
[29] Liao H, Hafner JH. Gold nanorod bioconjugates. Chem Mater 2005;17:4636–41.
[30] Chen YS, Frey W, Kim S, Kruizinga P, Homan K, Emelianov S. Silica-coated gold nanorods as photoacoustic signal nanoamplifiers. Nano Lett 2011;11:348–54.
[31] Wang F, Cheng S, Bao Z, Wang J. Anisotropic overgrowth of metal heterostructures induced by a site-selective silica coating. Angew Chem Int Ed Engl 2013;52:10344–8.
[32] Templeton AC, Pietron JJ, Murray RW, Mulvaney P. Solvent refractive index and core charge influence on the surface plasmon absorbance of alkanethiolate monolayer-protected gold clusters. J Phys Chem B 2004;104:564–70.
[33] Tian L, Gandra CN, Abbas A, Singamaneni S. Gold nanorods as plasmonic nanotransducers: distance-dependent refractive index sensitivity. Langmuir 2012;28:17435–42.
[34] Novo C, Mulvaney P. Charge-induced Rayleigh instability in small gold rods. Nano Lett 2007;7:520–4.
[35] Nicolai SHA, Rubim JC. Surface-enhanced resonance Raman (SERR) spectra of methylene blue adsorbed on a silver electrode. Langmuir 2003;19:4291–4.
[36] Severino D, Junqueira HC, Gugliotti M, Gabrielli DS, Baptista MS. Influence of negatively charged interfaces on the ground and excited state properties of methylene blue. Photochem Photobio 2003;77:459–68.
[37] Fenton HJH. Oxidation of tartaric acid in presence of iron. J Chem Soc Trans 1894;65:899–911.
[38] Nicolai SHA, Rodrigues PRP, Agostinho SML, Rubim JC. Electrochemical and spectroelectrochemical (SERS) studies of the reduction of methylene blue on a silver electrode. J Electroanal Chem 2002;527:103–11.
[39] Xiao GN, Man SQ. Surface-enhanced Raman scattering of methylene blue adsorbed on cap-shaped silver nanoparticles. Chem Phys Lett 2007;447:305–9.
[40] Jana D, Mandal A, De G. High Raman enhancing shape-tunable Ag nanoplates in alumina: a reliable and efficient SERS technique. Appl Mater Interfaces 2012;4:3330–4.
[41] Le Ru EC, Blackie E, Meyer M, Etchegoin PG. Surface enhanced Raman scattering enhancement factors: a comprehensive study. J Phys Chem C 2007;111:13794–803.